

# CanFields: Consolidating 4D Dynamic Shapes from Raw Scans

Miaowei Wang  
University of Edinburgh  
M.Wang-123@sms.ed.ac.uk

Changjian Li  
University of Edinburgh  
Changjian.li@ed.ac.uk

Amir Vaxman  
University of Edinburgh  
avaxman@inf.ed.ac.uk

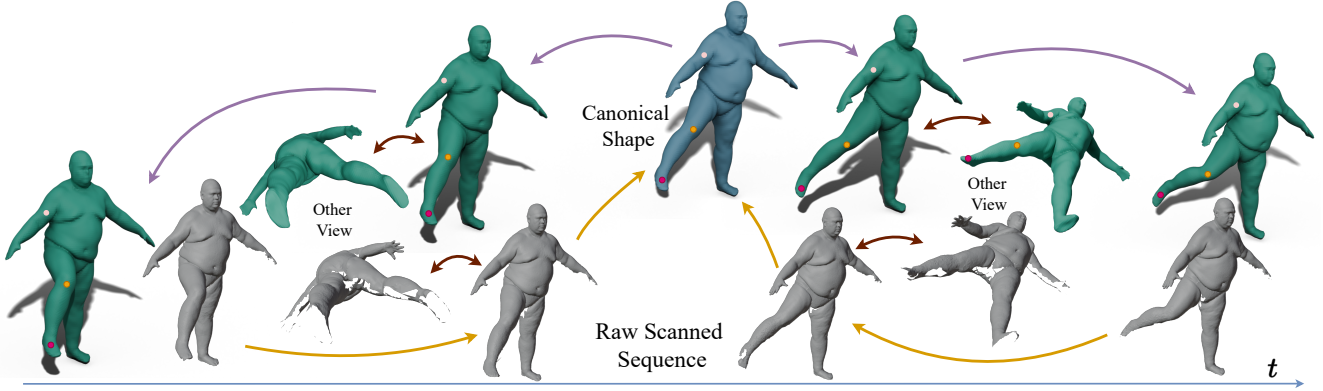


Figure 1. **CanFields** reconstructs a **canonical shape** by consolidating raw scanned sequence. We optimize the flow of the input sequence to the canonical time in an unsupervised manner. This results in a clean and topologically consistent representation of a time-continuous **deforming shape** where we can track any deforming point (dots). Our algorithm is robust to scanning defects (**mahogany** arrows). Our accompanying video shows the complete animation.

## Abstract

We introduce *Canonical Consolidation Fields* (CanFields), a new method for reconstructing a time series of independently captured 3D scans into a single, coherent deforming shape. This 4D representation enables continuous refinement across both space and time. Unlike prior methods that often over-smooth the geometry or produce topological and geometric artifacts, CanFields effectively learns geometry and deformation in an unsupervised way by incorporating two geometric priors. First, we introduce a dynamic consolidator module that adjusts the input and assigns confidence scores, balancing the learning of the canonical shape and its deformations. Second, we use low-frequency velocity fields to guide deformation while preserving fine details in canonical shapes through high-frequency bias. We validate the robustness and accuracy of CanFields on diverse raw scans, demonstrating its superior performance even with missing regions, sparse frames, and noise. Code is available in the supplementary materials and will be released publicly upon acceptance.

## 1. Introduction

Reproducing a real-world deformation, movement, or transformation digitally is a core task in geometry processing and physical simulation. For instance, motion capture systems [33] need to accurately reproduce the geometry of moving objects despite hidden or poorly scanned regions (Fig. 1). Correct tracking is vital in learning and reproducing the natural motions [18, 78] of objects and living beings. In medical imaging, modeling a dynamic object with a coherent mesh helps assess volume changes and deformation [7]. Autonomous driving systems require precise and rapid evaluation of the location and pose of moving entities [60].

The central challenge in these tasks, which our paper addresses, is obtaining a time-continuous representation of dynamic geometry, for tracking individual points and measuring deformation effects, such as metric and volume changes. Representing this using a single coherent deforming digital object is highly valuable, as it ensures accurate geometry reconstruction and minimizes artifacts from incomplete or noisy scans. We consider time-sequenced independent discrete samples, which may result from scanning or video tracking of a deforming object. Existing methods (see Sec. 2) fall into two categories. 4D Implicit methods

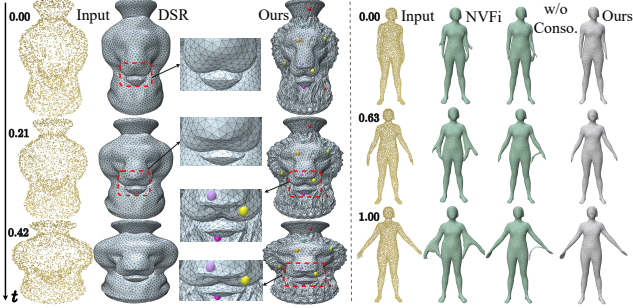


Figure 2. **Left:** Our method achieves temporally coherent meshing and accurate point tracking, surpassing purely implicit methods (like DSR [58]), which over-smooth results and lack time coherency. **Right:** Our approach is more robust to topological input artifacts than explicit flow-based methods (like NVFi [34]).

[42, 66, 69] create a space-time implicit function, in which time slices represent the deforming shapes. They handle topological changes naturally; however, the coupling of deformation and geometry tends to over-smooth details in the geometry (Fig. 2, left), and there is no explicit tracking of deforming points. Flow-based methods [6, 31, 61] reconstruct a canonical geometric shape and its deformation separately. This is a more difficult problem, as an incorrect reconstruction of the canonical shape leads to errors in the entire reconstructed sequence. This may include wrong topology (Fig. 2, right), where the hands are incorrectly attached to the body), or wrong geometry (Figs. 8 and 9).

Our approach is of the latter category, where we combine an *implicit* representation of the object in a canonical, static state with an *explicit* representation of the velocity field to capture instantaneous deformations. A key challenge in this paradigm is the simultaneous training of both the canonical shape and the deformation. This challenge arises because the training of the implicit canonical shape often prematurely converges to an incorrect outcome, as the flow training fails to properly integrate information across frames. Consequently, the resulting canonical shape (see Fig. 3) is a *chimera* with inconsistencies between different frames. To address the problem of jointly constructing shape and deformation, we introduce two novel strategies:

- **Dynamic Consolidation.** We introduce a dynamic consolidator module that balances the canonical shape and deformation learning. It introduces a learnable displacement of the input that facilitates time-wise coherency, and consequently infers topology and geometry correctly.
- **Low-High Frequency Bias Decoupling.** We encode the geometric details of the canonical shape with high frequencies, and the deformation field using low frequencies. This decoupling reproduces intricate details in the shape, alongside a smooth and physical deformation. It further enables a focused lightweight deformation field design, which is computationally efficient (see Tab. 3).

Our method significantly outperforms the state-of-the-art

(SOTA) methods, especially in the presence of considerable noise, missing regions, and ambiguous topology. We validate through extensive ablation and with real scanned data. We introduce the dynamic consolidator in Sec. 4, and the velocity field construction in Sec. 5. We detail the full pipeline in Sec. 6 and Fig. 7.

## 2. Related Work

**4D Reconstruction** The well-studied case of *static* point-cloud reconstruction (e.g., [4, 10, 13, 14, 20, 22, 28, 43, 54, 68, 70]) is not directly generalizable to 4D reconstruction. The challenge of considering 4D reconstruction has been attempted for several modalities. Works [8, 27, 34, 36–38, 45, 63, 65, 69] process dynamic scenes captured as *video frames* rendered by NeRF [27, 42, 69] or Gaussian Splatting [6, 26, 38, 72]. Videos capture high-frequency changes in motion and texture, but reconstructing coherent geometry from them is challenging. Point clouds [1, 31, 53, 61, 66], RGBD-based inputs [15] based on SDF [2, 15, 58, 59], or occupancy fields [9, 24, 46, 61, 66] are more suited for representing geometry. Scanned point clouds are susceptible to noise and missing data, particularly in dynamic scenes. We classify reconstruction methods into 4D Implicit and Flow-based categories, depending on whether they explicitly model deformation.

**4D Implicit** methods [2, 8, 15, 36, 42, 58, 66, 69] model dynamic sequences as spatiotemporal 4D functions. The shape at a given time point is then a time slice. RFNet-4D [66] and Li et al. [36] build correspondence by predicting deformation fields through additional decoders. SDF Flow [42] captures scene motion from multi-view videos by addressing linear equations with time derivatives. Additionally, GenCorres [71] (for shape generation) and 4DRecons [15] maintain rigidity by employing normal direction equations, utilizing meshes extracted via the marching cubes [40]. Atzmon et al. [2] introduces a Killing loss based on spatiotemporal second derivatives. We evaluate the state-of-the-art method in this category, DSR [58], extending DeepSDF [47] to 4D.

**Flow-based** methods [1, 6, 9, 17, 19, 23–25, 27, 31, 32, 34, 37, 38, 45, 46, 53, 59, 61, 67] model the explicit deformation of the geometry which is often represented as a canonical shape [24, 34, 38, 46, 52, 59]. The flow-based paradigm is also utilized in various tasks, including dense correspondence [3, 17, 19, 23], shape deformation from source to target [19, 25, 67, 74], motion transfer [23, 44], and shape generation [39]. We categorize these methods by how they represent the canonical shape: Predefined-template flow versus Learned-Canonical Flow.

**Predefined-template Flow** methods transform an *input* canonical shape into other frames or shapes. This includes well-established templates like SMPL for human bodies [5, 41, 50, 76], MANO for hands [30, 64], spheres for zero-



genus objects [67], or a reconstructed shape from the initial frame [63]. The reconstructed shape can either supervise the deformation network directly without additional training [45] or be jointly trained with the deformation network [6, 9, 32, 37, 61, 72]. Earlier methods, such as AMA [65], employed linear blend skinning (LBS) to deform articulated human templates from multi-view videos, while SCAPE [1] applied rotation matrices derived from 3D scans for template deformation. Recent approaches focus on pose-dependent clothed humans [41, 50, 76], moving away from minimal clothing setups [5]. The state-of-the-art method, Motion2VecSets [9], utilizes a diffusion model [75] to predict motion latent codes, combining them with initial frame shape codes for reconstruction. However, the numbers of frames in their input and output are fixed (and commensurate with the architecture of the network) and do not allow for continuous interpolation.

**Learned-Canonical Flow** methods [24, 27, 34, 46, 52, 59] learn the canonical shape alongside the deformation, as we do. Zhang et al. [74] introduce Hierarchical Rigid Constraints for shape deformation. SCANimate [52] employs learned-canonical flow to determine skinning weights for diverse human cloth shapes. Methods utilizing nearest neighbor search [17, 23] in canonical space facilitate correspondences between deformed shapes. To avoid such searches and achieve smooth morphing, forward mappings are introduced and combined with backward flow, leading to invertible flows (e.g., CaDeX [31], which learns deformation embeddings without interpolation, supervised by large datasets) or bijective mappings (e.g., Bednarik et al. [3] for pairwise correspondences; DG-Mesh [38] for coherent dynamic meshes from video). These methods often require cycle consistency regularization [31, 38]. **Neural ODE** [11] provides a streamlined approach by modeling a single velocity network for bidirectional deformation via integration, eliminating the need for dual networks. Neural ODEs have been applied in 4D reconstruction [24, 34, 46, 59], physical PDEs (ENF [29]), shape deformation (ShapeFlow [25]), and motion transfer (TemporalJacobian [44]). Their disadvantage is that their numerical integration impairs the convergence of the canonical shape during training. Our dynamic consolidator module alleviates these issues, while our velocity field design filters out high-frequency motion noise from the input sequence.

### 3. Temporally-Coherent Reconstruction

Our input comprises a time sequence of 3D shapes that sample an unknown, deforming closed 2-manifold  $S(t)$  with constant topology, sampled independently at each frame without correspondences. The samples could be partial and contain noise. These shapes are often (and in our datasets) the result of motion capture devices, that often preliminary and loosely mesh the shape at each time frame with-

out considering temporal coherence. We focus on closed objects that maintain consistent topology during deformation (e.g., moving people or animals) and assume that these samples represent the same object despite noise and missing data. Other than topology, our working assumption is that the objects are physical shapes that transform more or less elastically or isometrically. If not already provided as point clouds, our preprocessing step involves the Poisson disk sampling [16] of the shapes into a sequence of  $N$  point clouds  $\Omega = \{\Omega_i\}$ , where  $\Omega_i = \{\mathcal{P}_i, \mathcal{N}_i, t_i\}$  consists of points  $\mathcal{P}_i = \{x_{i,j} \in \mathbb{R}^3\}$ , corresponding normals  $\mathcal{N}_i = \{n_{i,j} \in \mathbb{S}^2\}$ , and timestamps  $t_i \in [0, 1]$ . The **output** is a function  $f(x, t) : \mathbb{R}^3 \times \mathbb{R} \rightarrow \mathbb{R}$  representing  $S(t)$  via zero sets:  $S_t = \{x \mid g_t(x) = 0\}$  where we define the single frame function  $g_t(x) \equiv f(x, t)$ .

In our setting, the implicit function  $f$  is decoupled into two components: the implicit *canonical function*  $g_c(x) : \mathbb{R}^3 \rightarrow \mathbb{R}$  at the canonical time  $t = c$ , with the *canonical shape*  $S_c = g_c^{-1}(0)$ , and the *flow function*  $\phi(x, t \mapsto c)$ , which maps a point  $x$  from any time  $t$  to the canonical time  $c$ .  $f$  is then defined by the pullback of  $g_c$  by  $\phi$ :

$$f(x, t) = g_c \circ \phi(x, t \mapsto c), \quad (1)$$

where  $c = 0.5$  in our setting. We parameterize the flow function  $\phi$  by a velocity field  $v(x, t) : \mathbb{R}^3 \times \mathbb{R} \rightarrow \mathbb{R}^3$  for each point  $x$  at time  $t$ , solving an initial value problem (IVP)  $\frac{\partial \phi(x, t)}{\partial t} = v(\phi(x, t), t)$  using a differential ODE solver [12]. This means that we can generate a continuous flow between any two times, by numerically integrating over the entire interval in between. We can then generate backward and forward flows without maintaining cycle consistency [31, 38]. During the evaluation, we apply the inverse mapping  $\phi(x, c \mapsto t)$  to flow the canonical shape through time by reversing the integration with the same velocity field  $v$ . We train  $f$  (which amounts to training both  $g_c$  and  $v$  simultaneously) with the following two losses:

$$\begin{aligned} E_{\text{fit}}(i) &= \mathbb{E}_{x_{i,j} \in \mathcal{P}_i} (|f(x_{i,j}, t_i)|^2 + \lambda_n \|\nabla f(x_{i,j}, t_i) - n_{i,j}\|^2), \\ E_{\text{eik}}(i) &= \mathbb{E}_{q \in \mathcal{Q}_i} (\|\nabla f(q, t_i)\| - 1)^2. \end{aligned} \quad (2)$$

The first is a fitting term, where  $n_{i,j}$  is the normal at point  $x_{i,j}$ , and  $\lambda_n = 0.1$  balances the point and normal fitting terms. The second is an Eikonal loss to make each  $f(x, t_i)$  an SDF. This is trained on a set of ambient samples  $\mathcal{Q}_i$  per time frame in the unit bounding box, where  $\mathcal{Q}_i$  includes 10K uniformly sampled points and 10K Gaussian samples near the point cloud. The Gaussian is a mixture of  $\mathcal{N}(0, \sigma_1^2 I)$  and  $\mathcal{N}(0, \sigma_2^2 I)$ , with  $\sigma_1^2$  as the distance to the 10<sup>th</sup> closest point and  $\sigma_2 = 0.3$  [2].

**The geometry & flow training problem.** The basic fitting as described above is inherently ill-defined [24, 34, 46], as it tries to fit the velocity field through a canonical shape

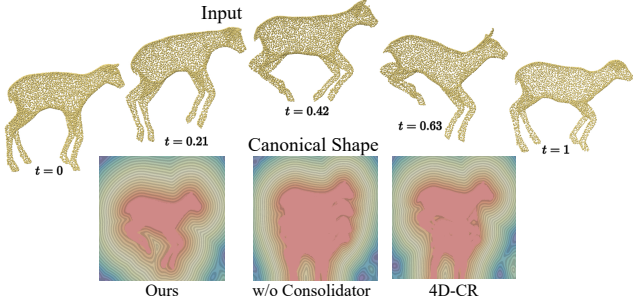


Figure 3. Dynamic consolidator  $\Upsilon$  effectively resolves conflicts to produce a correct canonical shape during simultaneous fitting, even for rapidly-deforming shapes, and where 4D-CR [24] fails.

trained simultaneously without additional supervision; for instance, instant velocity information or dense correspondences between frames. As a result, any inaccuracy in the canonical fitting or the velocity field easily manifests throughout the entire 4D reconstruction. A common example of such an artifact is an inaccurate registration of the flow-advection point clouds at the canonical time, which results in a shape that is a superposition of several shapes at once (see Fig. 3). A chief reason is that the numeric integration of velocity fields  $v$  through an ODE solver causes the flow function  $\phi$  to train much slower than the canonical implicit function  $g_c$ . As  $g_c$  converges, an underfitted  $\phi(x, t \mapsto c)$  may advect mismatched features—especially from frames distant from the canonical time—leading to local minima and artifacts in the canonical shape. This problem is more pronounced for rapidly-deforming shapes or noisy data. Backward-flow methods that acknowledge this issue [46, 48, 51, 59] typically adjust the learning rate to balance deformation and canonical shapes. However, this heuristic can adversely affect convergence rates. 4D-CR [24] enhances reliability by giving greater weight to frames at canonical time. However, problems with fast deforming motions remain unresolved, as illustrated in Fig. 3. We next introduce an adaptive mechanism that balances the training gap, by suppressing erroneous advected features and assessing their confidence during training.

#### 4. Dynamic Consolidator Module

Inspired by electric transformers that adjust voltage and current to meet an appliance’s input requirements, we introduce a learnable transformation of the input operating *before the ODE solver*, coupled with a confidence-based weighting to dynamically reduce the influence of outliers during fitting. Formally, we propose a dynamic consolidator module  $\Upsilon : \mathbb{R}^4 \rightarrow \mathbb{R}^4$  with two outputs:

$$\Upsilon : (\eta_{i,j} | \theta_i) \rightarrow (x_{i,j} + \delta_{i,j}, p_{i,j}) \quad (3)$$

where  $\eta_{i,j} = (x_{i,j}, t_i)$  is the space-time coordinate of point  $j$  in cloud  $\mathcal{P}_i$ , and  $\theta_i \in \mathbb{R}^{128}$  is a learnable latent code for

this cloud. One branch  $\delta$  of the consolidator module  $\Upsilon$  outputs a spatial deviation function  $\delta_{i,j} = \delta(x_{i,j})$  applied to the raw data input. The other branch  $p$  provides a confidence score function  $p_{i,j} = p(x_{i,j}) \in [0, 1]$  for each input point  $x_{i,j}$ . Consequently, the function  $f$  is redefined as:

$$\hat{f}(x, t) = g_c \circ \phi(x + \delta, t \mapsto c). \quad (4)$$

The deviation  $\delta$  homogenizes the input points, to facilitate the consolidation of the points through the flow into the canonical time, for fitting  $g_c$ . The confidence  $p_{i,j}$  measures the reliability at that point, with low confidence expected for outliers. We reformulate the fitting loss  $E_{\text{fit}}(i)$  as follows:

$$\hat{E}_{\text{fit}}(i) = \mathbb{E}_{x_{i,j} \in \mathcal{P}_i} \left[ p_{i,j} \left( |\hat{f}(x_{i,j}, t_i)|^2 + \lambda_n \|\nabla \hat{f}(x_{i,j}, t_i) - n_{i,j}\|^2 \right) \right] \quad (5)$$

**Regulating  $\Upsilon$ :** We regulate  $\delta$  both in magnitude and spatial smoothness, with the following two loss terms:

$$E_{\text{mag}}(i) = \mathbb{E}_{x_{i,j} \in \mathcal{P}_i} \|\delta_{i,j}\|^2 \quad (6)$$

$$E_{\text{var}}(i) = \mathbb{E}_{x_{i,j} \in \mathcal{P}_i} \|\nabla \delta_{i,j}\|_F^2 \quad (7)$$

We also use a log-likelihood loss to encourage to fit *all* points from the raw consecutive frames:

$$E_{\text{log}}(i) = -\mathbb{E}_{x_{i,j} \in \mathcal{P}_i} \log(p_{i,j}), \quad (8)$$

which is zero if and only if all confidences are 1.

**Canonical Energy.** The canonical fitting loss is defined as  $E_{\text{can}}(i) = \lambda_{\text{fit}} \hat{E}_{\text{fit}}(i) + \lambda_{\text{eik}} E_{\text{eik}}(i) + \lambda_{\text{mag}} E_{\text{mag}}(i) + \lambda_{\text{var}} E_{\text{var}}(i) + \lambda_{\text{log}} E_{\text{log}}(i)$ , where  $\lambda$  are hyperparameters.

**Why dynamic consolidation works.** Our dynamic consolidator module is a variant of *curriculum learning*. To minimize the fitting loss  $\hat{E}_{\text{fit}}$ , the consolidator  $\Upsilon$  decreases the confidence scores  $p$  and deforms (smooths) the raw point cloud by increasing  $\delta$ . This in turn produces a smoother motion by focusing primarily on easier inputs with higher  $p$ . As training progresses, the regularization weights  $\lambda_{\text{mag}}$ ,  $\lambda_{\text{var}}$ , and  $\lambda_{\text{log}}$  are gradually increased. This counters the deformation and confidence scores and eventually encourages the model to better fit the original points and motion over time. As such, it moderates the fitting of  $g_c$ , allowing  $\phi$  to train more correctly. As the flow is trained more gradually, we get an accurate fitting of the canonical shape, mitigating missing regions and noise. This is apparent in all our results (see Figs. 2, 8 and 9 and Tab. 1). We provide the parameter scheduling in the Supplementary.

#### 5. Decoupling Low and High-Frequency Bias

**Frequency decoupling** is critical for capturing fine geometric details while ensuring smooth, physically plausible deformations over time (refer to the ablation studies in

Tab. 2 and Fig. 4, both conducted on the DeformingThings4D [35] dataset). High-frequency canonical geometry encoding  $g_c$  (Fig. 4, top) preserves fine details and avoids over-smoothing. Encoding deformation with low-frequency velocity ensures smooth, gradual deformations, preventing abrupt changes that degrade mesh quality (Fig. 4, bottom).

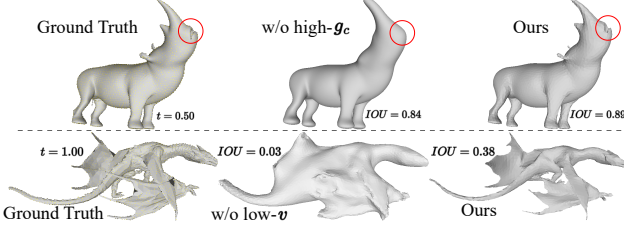


Figure 4. High-frequency  $g_c$  recovers fine details (e.g., mouth in rhinoDJ7S\_action3, top), while low-frequency  $v$  prevents kinks and registration errors (dragonQKS\_act18, bottom). See ablation in 7.3 for details.

### 5.1. Velocity Field Design

We assume that velocity varies smoothly in space and time. As shown in Fig. 5, we encode space-time coordinates with Random Fourier Features (RFF) defined as  $\gamma(\eta) = [\cos(b_1^T \eta), \sin(b_1^T \eta), \dots, \cos(b_{d/2}^T \eta), \sin(b_{d/2}^T \eta)]$ , with coefficients  $\{b_i\}$  sampled from a Gaussian distribution with variance  $\sigma = 0.4$ ; this filters out high-frequency kinks and abrupt changes. This encoding is processed through two MLP layers,  $\zeta_A$  and  $\zeta_B$ , to capture a mixture of low- and medium-frequency velocities in the composition:  $\zeta_{LM}(\eta) = w_M \zeta_A(\gamma(\eta)) + w_L \zeta_B(\zeta_A(\gamma(\eta)))$ . Here,  $\zeta_B \circ \zeta_A$  serves as a low-frequency component—using it alone (i.e.,  $w_M = 0$ ) loses detail, while relying solely on  $\zeta_A$  (i.e.,  $w_L = 0$ ) misses global motion. The optimal average weights  $w_L = w_M = 0.5$  effectively preserve both aspects (see Supplementary for ablations).

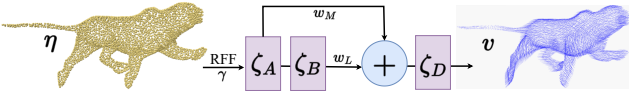


Figure 5. Our velocity field integrates positional encoding  $\gamma$  with low- and medium-frequency components  $\zeta_B$  and  $\zeta_A$  controlled by weights  $w_M$  and  $w_L$ , followed by a decoder layer  $\zeta_D$  to produce a spatial velocity field, all implemented as single MLP layers.

Finally, a coordinate-based velocity decoder (single MLP layer)  $\zeta_D : \mathbb{R}^h \rightarrow \mathbb{R}^3$  converts the output of  $\zeta_{LM}$  from Fourier frequency space into the 3D velocity field  $v \in \mathbb{R}^3$ . This minimal design reduces the parameter search space, facilitates global optimization, and *accelerates* ODE integration, resulting in significant time savings (see Tab. 3).

### 5.2. Velocity Regularization

We assume that the velocity field represents the physical motion of solid or articulated objects, favoring isometric or elastic deformations. By modeling velocity as an explicit

variable—unlike methods that model flow directly [2]—we only need to compute its first spatial ( $\nabla$ ) or temporal ( $\frac{\partial}{\partial t}$ ) derivatives, which are more stable and easily obtained using PyTorch Autograd [49]. We use the following losses:

⇒ **Dirichlet Energy:**  $E_{\text{diri}}(i) = \frac{1}{2} \mathbb{E}_{x_{i,j} \in \mathcal{P}_i} \|\nabla v(x_{i,j}, t_i)\|_F^2$  controls spatial variation to force incompressible flow [53].

⇒ **Consistent Speed:**  $E_{\text{speed}}(i) = \frac{1}{2} \mathbb{E}_{x_{i,j} \in \mathcal{P}_i} \left\| \frac{\partial v(x_{i,j}, t_i)}{\partial t} \right\|^2$  penalizes sudden movements in unevenly spaced frames and prevents *singularities* (vanishing gradients and zero velocity), especially in sparse or slow-motion frames.

⇒ **Hierarchical Isometry:** We introduce two regularizations for isometry: the Killing loss (Eq. (9)) ensures *pointwise* elastic motion, while articulated rigidity [2, 74] (Eq. (10)) focuses on *piecewise* rigidity.

The **Killing energy** [56, 57, 62] is a 1<sup>st</sup>-order approximation for isometry, defined as:

$$E_{\text{kill}}(i) = \frac{1}{2} \mathbb{E}_{x_{i,j} \in \mathcal{P}_i} \|\nabla v(x_{i,j}, t_i) + \nabla v(x_{i,j}, t_i)^T\|_F^2. \quad (9)$$

We also adapt a motion-segmentation network  $\zeta_H$  [2, 74] for quasi-articulated systems, with  $\zeta_H : \mathbb{R}^3 \rightarrow [0, 1]^H$  outputting probabilities  $\zeta_{H,h}(x)$  for point  $x$  to be in segment  $h$ . With this, we introduce **Articulated rigidity** defined as:

$$E_{\text{rigid}}(i) = \mathbb{E}_{x_{i,j} \in \mathcal{P}_i} \sum_{h \in [1, H]} \zeta_{H,h}(\phi(x_{i,j}, t_i \mapsto c)) \cdot \|(R_{h,i} x_{i,j} + \tau_{h,i}) - \phi(x_{i,j}, t_i \mapsto c)\|^2, \quad (10)$$

with the rigid transformations  $\{R_{h,i} \in SO(3), \tau_{h,i} \in \mathbb{R}^3\}$  computed via SVD (see Supplementary). This training also yields a motion segmentation of the moving object based on the highest point probability (see Fig. 6). **Note:**  $\zeta_H$  operates on the consolidated canonical space, and thus  $E_{\text{rigid}}$  is robust to features disappearing in time frames.

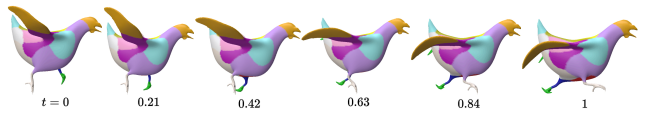


Figure 6. The motion-segmenter  $\zeta_H$  learns the object’s articulation by segmenting its (softly) piecewise-rigid parts (see colors).

The total velocity regularization is  $E_{\text{velo}}(i) = \lambda_{\text{rigid}} E_{\text{rigid}}(i) + \lambda_{\text{kill}} E_{\text{kill}}(i) + \lambda_{\text{diri}} E_{\text{diri}}(i) + \lambda_{\text{speed}} E_{\text{speed}}(i)$ , where  $\lambda$  are hyperparameters with multi-stage scheduling (see Supplementary) to avoid *local minima*.

## 6. Training and Testing

**Training Pipeline** Illustrated in Fig. 7 (top), our training architecture trains the velocity network  $v$  and the canonical shape function  $g_c$ . The key components are: the dynamic consolidator module  $\Upsilon$  for coherent fitting (Sec. 4), a low- and medium-frequency velocity network  $v$



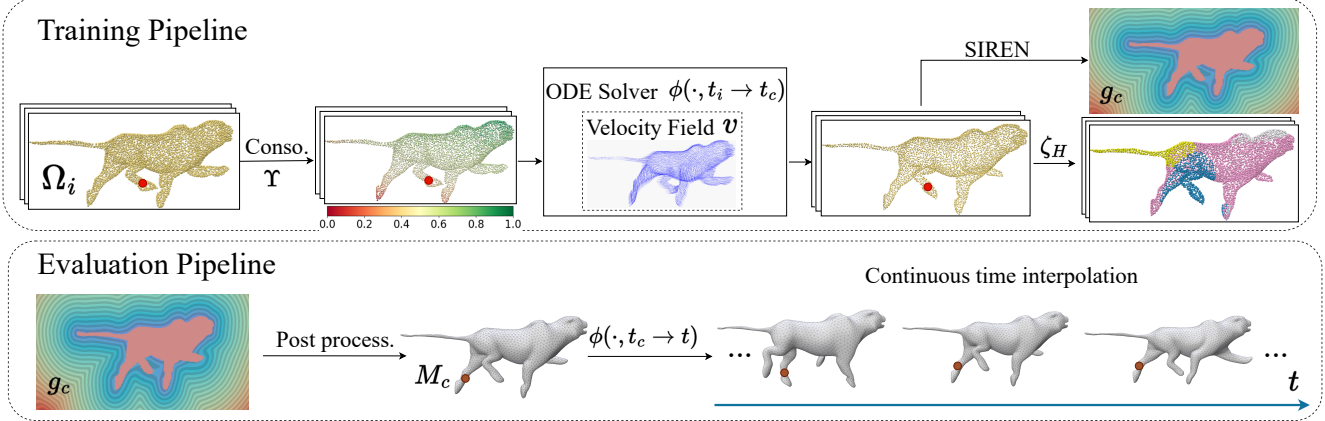


Figure 7. In the training phase, input point clouds  $\Omega = \{\Omega_i\}$  are processed by the learnable dynamic consolidator module  $\Upsilon$ , which reduces variance and scores confidence. The modified points are then sent through the learnable velocity network  $v$  to an ODE solver, producing the flow  $\phi$  that transforms points to the canonical time  $t = c$ . A learnable motion-segmentation network  $\zeta_H$  segments the points to reveal articulation, and the implicit canonical function  $g_c$  is reconstructed with SIREN encoding. Our evaluation pipeline extracts the zero set  $S_c$  of  $g_c$  using marching cubes, remeshes it to the desired discretization  $M_c$ , and flows its vertices into the shape  $M_t$  for any prescribed time  $t$ .

that models smooth deformations (Sec. 5), a *high-frequency* canonical function computed with SIREN [55], and a motion-segmentation network  $\zeta_H$  for articulated deformation (Eq. (10)). The *total energy* across the entire input sequence is  $E = \sum_i E(i)$  with  $E(i) = E_{\text{can}}(i) + E_{\text{velo}}(i)$ .

**Evaluation Pipeline** Having fitted  $v$  and  $g_c$ , we can generate  $S(t)$  for any  $t \in [0, 1]$  (Fig. 7, bottom). We first create a mesh  $M_c$  to discretize the canonical shape  $S_c$  using marching cubes [40] and remesh [21] it to any desired mesh. We then flow the vertices of  $M_c$  through  $\phi$  with the ODE solver to obtain  $M(t)$ , a discrete representation of  $S(t)$ .

## 7. Results and Evaluation

We present the main results and evaluations. The Supplementary provides additional experimental results and analyses, and complete implementation and scheduling details. It also includes potential applications (consolidating raw textures, dynamic texture generation, arbitrary mesh discretization), robustness evaluations (without normals, noisy points, sparse points, and sparse frames), and limitations (topological changes, rapid transitions, and finer details).

**Benchmark:** We qualitatively evaluate *raw scan* reconstruction with the human dataset DFAUST [5] (no corresponding ground-truth 3D shape). For more diverse dynamic *interpolation* and quantitative evaluations, we use DeformingThings4D [35] (varied animals and motions) and CAPE [50] (real clothed human motion).

**Baselines:** We compare with SOTA approaches, adapting them as needed. 1) **NDF** [59] introduces a quasi-time-varying velocity field and employs DeepSDF [47] for canonical shape representation. 2) **DSR** [58] predicts SDF values from spacetime input without explicit deformation. 3) **OFlow** [46] velocity network is adapted by using two

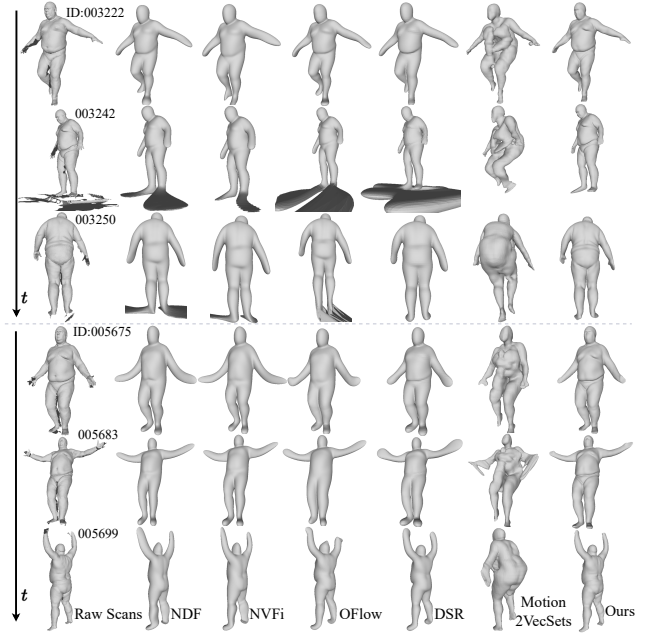


Figure 8. Reconstruction from **raw** scans. Our method outperforms others with significantly fewer artifacts on *one\_leg\_loose* (top) and *jumping-jacks* (bottom) from DFAUST (Subject ID = 50002) [5], including mesh indices (ID). Some visualizations exceed display bounds and are cropped. See the supplementary video for full details.

learnable latent codes for single-shape fitting. 4) **NVFi** [34] uses a special encoding in velocity for rigid regularization from multi-view video, which we integrate into NDF’s pipeline. 5) **Motion2VecSets** [9], the recent supervised method, uses fixed-length (17 frames) input and output without interpolation, limiting its application to evaluating our raw scan reconstruction task. All methods, except DSR and Motion2VecSets, are flow-based, utilizing a

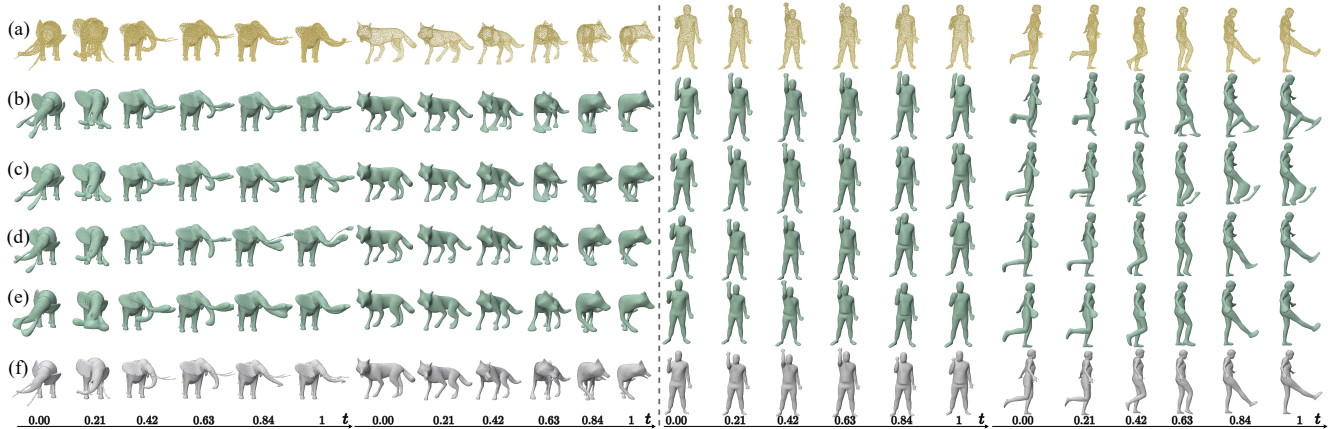


Figure 9. 4D interpolation results for synthetic animal motions from the DeformingThings4D [35] dataset (left) and registered real clothed human motions from the CAPE dataset [50] (right). (a) Input, (b) NVFi [34], (c) NDF [59], (d) OFlow [46], (e) DSR [58], (f) Ours. Our method captures natural temporal deformations with precise details, avoiding over-smoothing and artifacts (see Supplementary video).

canonical shape that evolves over time. In contrast to these approaches, which use DeepSDF, we employ SIREN.

**Metrics:** We exploit mean Intersection-over-Union (**IoU**), Chamfer L1-Distance (**CD**), and Normal Consistency (**NC**) as evaluation metrics. We report mean and worst scores along the temporal axis for a more rigorous assessment.

### 7.1. Raw Scans Reconstruction

The DFAUST dataset contains a raw-scan version, retaining all outliers and irrelevant objects (e.g., the standing ground), making it a challenging and more practical benchmark for reconstruction performance evaluation. We present a qualitative evaluation in Fig. 8 with three discrete reconstructed frames. It is clear that all SOTA flow-based or implicit model-based methods suffer from severe missing regions and outliers, while our method can faithfully reconstruct each frame. We note that, for a fair comparison, we train almost all methods with a single sequence, like ours. The exception is Motion2VecSet which is a pre-trained diffusion model. Thus, it by design underperforms on raw scans without having been trained on corresponding ground truths.

### 7.2. 4D Interpolation Reconstruction

We perform a quantitative evaluation of continuous interpolation methods (which means we exclude Motion2VecSets). To perform the interpolation quantitative evaluation, we clip and downsample frames from the benchmark datasets to which we have ground truth baselines (CAPE and DeformingThings4D). We create input sequences of 10 to 25 frames. For each sequence, we interpolate 50 frames from  $t = 0$  to  $t = 1$ , evaluating them against the nearest ground truth mesh, assuming negligible differences (as in [58, 59, 73]). In Tab. 1, our method outperforms others in all metrics for both synthetic animal and real human motion datasets. Visual comparisons in Fig. 9 demonstrate our method’s superior temporal coherence. Our combina-

tion of input consolidation and frequency decoupling effectively reproduces the ground truth. In contrast, the velocity networks for NDF and NVFi struggle to align parts in fast, complex sequences, while OFlow with a deep velocity network and DSR perform better. However, DSR’s single SDF network leads to oversmoothing and detail loss, especially in complex objects (see the cases in Figs. 2 and 9).

Table 1. Quantitative results on the DeformingThings4D [35] and CAPE [41] datasets for interpolation reconstruction, with the best methods and metrics highlighted.

Dataset	Method	IoU (%)		CD ( $\times 10^{-4}$ )		NC ( $\times 10^{-2}$ )	
		Mean $\uparrow$	Min $\uparrow$	Mean $\downarrow$	Max $\downarrow$	Mean $\uparrow$	Min $\uparrow$
Li et al. [35]	NDF [59]	74.43	58.45	14.20	70.40	75.82	68.27
	DSR [58]	75.26	69.50	6.762	15.81	77.59	72.68
	OFlow [46]	78.47	71.56	8.012	32.28	77.17	72.37
	NVFi [34]	75.59	68.95	12.00	44.12	75.50	71.50
	<b>Ours</b>	<b>82.84</b>	<b>74.12</b>	<b>4.606</b>	<b>15.28</b>	<b>78.21</b>	<b>73.37</b>
Ma et al. [41]	NDF [59]	79.55	59.30	14.03	84.71	82.96	73.76
	DSR [58]	80.23	77.42	10.13	14.38	83.35	81.93
	OFlow [46]	77.15	73.38	28.55	35.00	81.61	80.08
	NVFi [34]	81.50	75.73	21.62	25.39	82.85	80.73
	<b>Ours</b>	<b>84.17</b>	<b>80.94</b>	<b>6.554</b>	<b>11.23</b>	<b>84.98</b>	<b>83.06</b>

Table 2. Quantitative ablations for the impact of dynamic consolidator ( $\Upsilon$ ), high-frequency canonical shape (high- $g_c$ ), low-frequency velocity field (low- $v$ ), and articulated rigidity ( $E_{\text{rigid}}$ ).

Method	IoU (%)		CD ( $\times 10^{-4}$ )		NC ( $\times 10^{-2}$ )	
	Mean $\uparrow$	Min $\uparrow$	Mean $\downarrow$	Max $\downarrow$	Mean $\uparrow$	Min $\uparrow$
<b>Default</b>	<b>83.23</b>	<b>78.34</b>	<b>2.193</b>	<b>7.481</b>	<b>82.22</b>	<b>78.49</b>
w/o $\Upsilon$	57.98	35.74	171.2	544.2	67.73	57.39
w/o high- $g_c$	60.20	57.60	496.2	630.0	75.65	73.08
w/o low- $v$	81.00	75.04	7.783	37.75	80.67	76.14
w/o $E_{\text{rigid}}$	73.07	65.19	662.7	2473	78.35	74.57

### 7.3. Analysis and Ablation

**Missing Regions.** To assess our method’s capability to aggregate partial information from different frames, we manu-

ally crop various regions in the input frames. In Fig. 10, our explicit velocity field modeling and regularization enable the complete recovery of the canonical frame by advecting details from the raw sequence, while DSR failed to recover the missing parts (see Suppl. for quantitative measures).

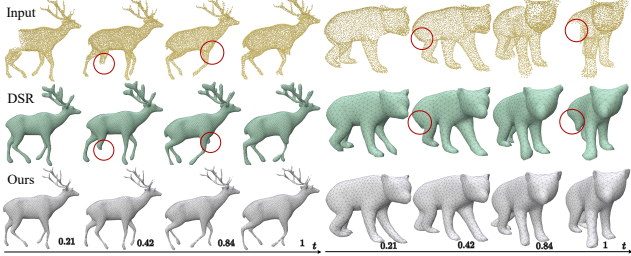


Figure 10. Our method (gray) correctly recovers geometry and deformation from missing regions, while DSR (green) misses them.

**Quantitative Ablations.** We evaluate the contribution of our key modules in Tab. 2: dynamic consolidator ( $\Upsilon$ ), high-frequency canonical shape ( $g_c$ ), low-frequency velocity field ( $v$ ), and articulated rigidity ( $E_{\text{rigid}}$ ). We ablate these using five diverse sequences from DeformingThings4D (rhinoDJ7S\_action3, bearPDD\_swimforwardRM, foxYSY\_Crouchback, elephantLN0\_act3, foxXAT\_Rotate180R). Replacing high-frequency  $g_c$  (SIREN) with low-frequency shape representation (DeepSDF) results in poor shape recovery. Replacing  $v$  with NVFi’s velocity field slightly degrades performance, highlighting the stability of our low-frequency field. Without the consolidator, the training balance between  $g_c$  and  $v$  fails, leading to artifacts. Removing  $E_{\text{rigid}}$  causes rigid motion tracking errors.

**Velocity Regularization Ablation.** Killing energy  $E_{\text{kill}}$  is essential for accurately reproducing isometric and rigid motions. In Fig. 11 (left), we apply a rotation to a Genus-2 mesh from Thingi10K [77] (ID: 83024), and almost perfectly reproduce it with  $E_{\text{kill}}$ , while its absence introduces artifacts; *Dirichlet Energy*  $E_{\text{diri}}$  regulates spatial smoothness, effectively reproducing gentle wrist movements in Fig. 11 (middle); *speed-consistency*  $E_{\text{speed}}$  helps reproduces smooth motion Fig. 11 (right) even with three frames; DSR [58] struggles with near-isometric deformations, due to reliance on gradient-based movement.

**Efficiency.** We assess timings on an A100 80G GPU using sequence rabbit7L6\_HiderotL (see Tab. 3) and analyze velocity parameters. NVFi has fewer parameters, but its positional encoding calculation is more time-consuming. Our evaluation comprises extracting a mesh of the canonical shape via marching cubes and flowing it to 50 interpolated frames. DSR requires separate mesh extraction for each frame, increasing evaluation time. Our average time includes the computation of velocity derivatives, with peak GPU memory usage of 20GB during fitting. The fastest

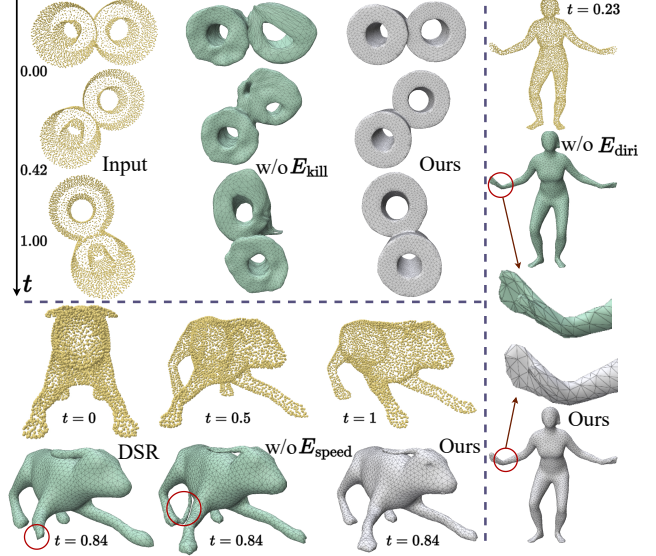


Figure 11. **Top:**  $E_{\text{kill}}$  reproduces rigid transformations, minimizing artifacts. **Middle:**  $E_{\text{diri}}$  preserves local shape during deformation (e.g., the right wrist). **Bottom:**  $E_{\text{speed}}$  facilitates smooth motion even with only three input frames. Artifacts are highlighted in red.

training is done by DSR, but they do not construct any temporal coherency, and thus solve a simpler problem. Our training time is slightly slower than that of the flow-based NDF, but our results are significantly better. Since we use smaller velocity networks, our evaluation time is the fastest.

Table 3. Timing Comparison. #velo is the number of learnable parameters in velocity networks. Fitting Time (FitTime) is averaged per 100 iterations, and Evaluation Time (EvalTime) is split into canonical shape generation  $M_c$  and flowing to other frames  $M_t$ .

Method	Category	#velo ↓	FitTime (s) ↓	EvalTime (s) ↓
DSR[58]	4D Implicit	-	<b>5.29</b>	251
OFlow[46]	ODE Flow	3,291,395	83.4	2.48 + 40.3
NDF[59]	ODE Flow	1,591,564	27.0	2.47 + 17.5
NVFi[34]	ODE Flow	<b>70,534</b>	36.2	2.47 + 21.6
Ours	ODE Flow	285,187	30.1	<b>1.30 + 15.6</b>

## 8. Conclusion

In this work, we introduced a hybrid implicit-explicit framework for accurately reconstructing the geometry and motion of deforming objects. Our innovative consolidation process demonstrates significant promise in various applications, from motion capture to dynamic scene understanding. Looking ahead, integrating texture and exploring alternative input formats, such as videos, could enhance our approach and expand its applicability. We believe our method lays a strong foundation for future research in dynamic object reconstruction and offers exciting opportunities for automatic rigging and animation.



## References

- [1] Dragomir Anguelov, Praveen Srinivasan, Daphne Koller, Sebastian Thrun, Jim Rodgers, and James Davis. Scape: shape completion and animation of people. In *ACM SIGGRAPH 2005 Papers*, pages 408–416. 2005. [2](#), [3](#)
- [2] Matan Atzmon, David Novotny, Andrea Vedaldi, and Yaron Lipman. Augmenting implicit neural shape representations with explicit deformation fields. *arXiv preprint arXiv:2108.08931*, 2021. [2](#), [3](#), [5](#)
- [3] Jan Bednarik, Vladimir G Kim, Siddhartha Chaudhuri, Shaifali Parashar, Mathieu Salzmann, Pascal Fua, and Noam Aigerman. Temporally-coherent surface reconstruction via metric-consistent atlases. In *Proceedings of the IEEE/CVF International Conference on Computer Vision*, pages 10458–10467, 2021. [2](#), [3](#)
- [4] Yizhak Ben-Shabat, Chamin Hewa Koneputugodage, and Stephen Gould. Digs: Divergence guided shape implicit neural representation for unoriented point clouds. In *Proceedings of the IEEE/CVF Conference on Computer Vision and Pattern Recognition*, pages 19323–19332, 2022. [2](#)
- [5] Federica Bogo, Javier Romero, Gerard Pons-Moll, and Michael J. Black. Dynamic FAUST: Registering human bodies in motion. In *IEEE Conf. on Computer Vision and Pattern Recognition (CVPR)*, 2017. [2](#), [3](#), [6](#)
- [6] Weiwei Cai, Weicai Ye, Peng Ye, Tong He, and Tao Chen. Dynasurfgs: Dynamic surface reconstruction with planar-based gaussian splatting. *arXiv preprint arXiv:2408.13972*, 2024. [2](#), [3](#)
- [7] Federico Canè, Benedict Verhegghe, Matthieu De Beule, Philippe B Bertrand, Rob J Van der Geest, Patrick Segers, Gianluca De Santis, et al. From 4d medical images (ct, mri, and ultrasound) to 4d structured mesh models of the left ventricular endocardium for patient-specific simulations. *BioMed research international*, 2018, 2018. [1](#)
- [8] Ang Cao and Justin Johnson. Hexplane: A fast representation for dynamic scenes. In *Proceedings of the IEEE/CVF Conference on Computer Vision and Pattern Recognition*, pages 130–141, 2023. [2](#)
- [9] Wei Cao, Chang Luo, Biao Zhang, Matthias Nießner, and Jiapeng Tang. Motion2vecsets: 4d latent vector set diffusion for non-rigid shape reconstruction and tracking, 2024. [2](#), [3](#), [6](#)
- [10] Jonathan C Carr, Richard K Beatson, Jon B Cherrie, Tim J Mitchell, W Richard Fright, Bruce C McCallum, and Tim R Evans. Reconstruction and representation of 3d objects with radial basis functions. In *Proceedings of the 28th annual conference on Computer graphics and interactive techniques*, pages 67–76, 2001. [2](#)
- [11] Ricky TQ Chen, Yulia Rubanova, Jesse Bettencourt, and David K Duvenaud. Neural ordinary differential equations. *Advances in neural information processing systems*, 31, 2018. [3](#)
- [12] Ricky T. Q. Chen. torchdiffeq, 2018. [3](#)
- [13] Zhang Chen, Yinda Zhang, Kyle Genova, Sean Fanello, Sofien Bouaziz, Christian Häne, Ruofei Du, Cem Keskin, Thomas Funkhouser, and Danhang Tang. Multiresolution deep implicit functions for 3d shape representation. In *Proceedings of the IEEE/CVF International Conference on Computer Vision*, pages 13087–13096, 2021. [2](#)
- [14] Zhi-Quan Cheng, Yanzhen Wang, Bao Li, Kai Xu, Gang Dang, and Shiyao Jin. A survey of methods for moving least squares surfaces. In *VG/PBG@ SIGGRAPH*, pages 9–23, 2008. [2](#)
- [15] Xiaoyan Cong, Haitao Yang, Liyan Chen, Kaifeng Zhang, Li Yi, Chandrajit Bajaj, and Qixing Huang. 4drecons: 4d neural implicit deformable objects reconstruction from a single rgb-d camera with geometrical and topological regularizations. *arXiv preprint arXiv:2406.10167*, 2024. [2](#)
- [16] Massimiliano Corsini, Paolo Cignoni, and Roberto Scopigno. Efficient and flexible sampling with blue noise properties of triangular meshes. *IEEE Transaction on Visualization and Computer Graphics*, 18(6):914–924, 2012. <http://doi.ieeecomputersociety.org/10.1109/TVCG.2012.34>. [3](#)
- [17] Yu Deng, Jiaolong Yang, and Xin Tong. Deformed implicit field: Modeling 3d shapes with learned dense correspondence. In *Proceedings of the IEEE/CVF Conference on Computer Vision and Pattern Recognition*, pages 10286–10296, 2021. [2](#), [3](#)
- [18] Jing Dong, John Gary Burnham, Byron Boots, Glen Rains, and Frank Dellaert. 4d crop monitoring: Spatio-temporal reconstruction for agriculture. In *2017 IEEE International Conference on Robotics and Automation (ICRA)*, pages 3878–3885. IEEE, 2017. [1](#)
- [19] Thibault Groueix, Matthew Fisher, Vladimir G Kim, Bryan C Russell, and Mathieu Aubry. 3d-coded: 3d correspondences by deep deformation. In *Proceedings of the european conference on computer vision (ECCV)*, pages 230–246, 2018. [2](#)
- [20] Rana Hanocka, Gal Metzer, Raja Giryes, and Daniel Cohen-Or. Point2mesh: a self-prior for deformable meshes. *ACM Trans. Graph.*, 39(4), 2020. [2](#)
- [21] Hugues Hoppe, Tony DeRose, Tom Duchamp, John McDondald, and Werner Stuetzle. Mesh optimization. In *Proceedings of the 20th annual conference on Computer graphics and interactive techniques*, pages 19–26, 1993. [6](#)
- [22] Jiahui Huang, Zan Gojcic, Matan Atzmon, Or Litany, Sanja Fidler, and Francis Williams. Neural kernel surface reconstruction. In *Proceedings of the IEEE/CVF Conference on Computer Vision and Pattern Recognition*, pages 4369–4379, 2023. [2](#)
- [23] Zeyu Huang, Honghao Xu, Haibin Huang, Chongyang Ma, Hui Huang, and Ruizhen Hu. Spatial and surface correspondence field for interaction transfer. *ACM Transactions on Graphics (Proceedings of SIGGRAPH)*, 43(4):83:1–83:12, 2024. [2](#), [3](#)
- [24] Boyan Jiang, Yinda Zhang, Xingkui Wei, Xiangyang Xue, and Yanwei Fu. Learning compositional representation for 4d captures with neural ode. In *Proceedings of the IEEE/CVF Conference on Computer Vision and Pattern Recognition*, pages 5340–5350, 2021. [2](#), [3](#), [4](#)
- [25] Chiyu Jiang, Jingwei Huang, Andrea Tagliasacchi, and Leonidas J Guibas. Shapeflow: Learnable deformation flows among 3d shapes. *Advances in Neural Information Processing Systems*, 33:9745–9757, 2020. [2](#), [3](#)

- [26] Xu Jiawei, Fan Zexin, Yang Jian, and Xie Jin. Grid4D: 4D decomposed hash encoding for high-fidelity dynamic scene rendering. *The Thirty-eighth Annual Conference on Neural Information Processing Systems*, 2024. 2
- [27] Erik C.M. Johnson, Marc Habermann, Soshi Shimada, Vladislav Golyanik, and Christian Theobalt. Unbiased 4d: Monocular 4d reconstruction with a neural deformation model. In *Proceedings of the IEEE/CVF Conference on Computer Vision and Pattern Recognition (CVPR) Workshops*, pages 6598–6607, 2023. 2, 3
- [28] Michael Kazhdan, Matthew Bolitho, and Hugues Hoppe. Poisson surface reconstruction. In *Proceedings of the fourth Eurographics symposium on Geometry processing*, 2006. 2
- [29] David M Knigge, David R Wessels, Riccardo Valperga, Samuele Papa, Jan-Jakob Sonke, Efstratios Gavves, and Erik J Bekkers. Space-time continuous pde forecasting using equivariant neural fields. *arXiv e-prints*, pages arXiv–2406, 2024. 3
- [30] Jihyun Lee, Junbong Jang, Donghwan Kim, Minhyuk Sung, and Tae-Kyun Kim. Fourierhandflow: Neural 4d hand representation using fourier query flow. In *NeurIPS*, 2023. 2
- [31] Jiahui Lei and Kostas Daniilidis. Cadex: Learning canonical deformation coordinate space for dynamic surface representation via neural homeomorphism. In *Proceedings of the IEEE/CVF Conference on Computer Vision and Pattern Recognition*, pages 6624–6634, 2022. 2, 3
- [32] Deqi Li, Shi-Sheng Huang, Zhiyuan Lu, Xinran Duan, and Hua Huang. St-4dgs: Spatial-temporally consistent 4d gaussian splatting for efficient dynamic scene rendering. In *ACM SIGGRAPH 2024 Conference Papers*, New York, NY, USA, 2024. Association for Computing Machinery. 2, 3
- [33] Jialian Li, Jingyi Zhang, Zhiyong Wang, Siqi Shen, Chenglu Wen, Yuexin Ma, Lan Xu, Jingyi Yu, and Cheng Wang. Lidarcap: Long-range marker-less 3d human motion capture with lidar point clouds, 2022. 1
- [34] Jinxi Li, Ziyang Song, and Bo Yang. Nvfi: Neural velocity fields for 3d physics learning from dynamic videos. *Advances in Neural Information Processing Systems*, 36, 2023. 2, 3, 6, 7, 8
- [35] Yang Li, Hikari Takehara, Takafumi Taketomi, Bo Zheng, and Matthias Nießner. 4dcomplete: Non-rigid motion estimation beyond the observable surface. In *Proceedings of the IEEE/CVF International Conference on Computer Vision*, pages 12706–12716, 2021. 5, 6, 7
- [36] Zhengqi Li, Simon Niklaus, Noah Snavely, and Oliver Wang. Neural scene flow fields for space-time view synthesis of dynamic scenes. In *Proceedings of the IEEE/CVF Conference on Computer Vision and Pattern Recognition*, pages 6498–6508, 2021. 2
- [37] Youtian Lin, Zuozhuo Dai, Siyu Zhu, and Yao Yao. Gaussian-flow: 4d reconstruction with dynamic 3d gaussian particle. In *Proceedings of the IEEE/CVF Conference on Computer Vision and Pattern Recognition (CVPR)*, pages 21136–21145, 2024. 2, 3
- [38] Isabella Liu, Hao Su, and Xiaolong Wang. Dynamic gaussians mesh: Consistent mesh reconstruction from monocular videos, 2024. 2, 3
- [39] Zhengzhe Liu, Jingyu Hu, Ka-Hei Hui, Xiaojuan Qi, Daniel Cohen-Or, and Chi-Wing Fu. Exim: A hybrid explicit-implicit representation for text-guided 3d shape generation. *ACM Transactions on Graphics (TOG)*, 42(6):1–12, 2023. 2
- [40] William E Lorensen and Harvey E Cline. Marching cubes: A high resolution 3d surface construction algorithm. In *Seminal graphics: pioneering efforts that shaped the field*, pages 347–353. 1998. 2, 6
- [41] Qianli Ma, Jinlong Yang, Anurag Ranjan, Sergi Pujades, Gerard Pons-Moll, Siyu Tang, and Michael J. Black. Learning to Dress 3D People in Generative Clothing. In *Computer Vision and Pattern Recognition (CVPR)*, 2020. 2, 3, 7
- [42] Wei Mao, Richard Hartley, Mathieu Salzmann, et al. Neural sdf flow for 3d reconstruction of dynamic scenes. In *The Twelfth International Conference on Learning Representations*. 2
- [43] Thomas Müller, Alex Evans, Christoph Schied, and Alexander Keller. Instant neural graphics primitives with a multiresolution hash encoding. *ACM Trans. Graph.*, 41(4):102:1–102:15, 2022. 2
- [44] Sanjeev Muralikrishnan, Niladri Shekhar Dutt, Siddhartha Chaudhuri, Noam Aigerman, Vladimir Kim, Matthew Fisher, and Niloy J Mitra. Temporal residual jacobians for rig-free motion transfer. In *Proceedings of the european conference on computer vision (ECCV)*, 2024. 2, 3
- [45] Armin Mustafa, Hansung Kim, Jean-Yves Guillemaut, and Adrian Hilton. Temporally coherent 4d reconstruction of complex dynamic scenes. In *Proceedings of the IEEE Conference on Computer Vision and Pattern Recognition (CVPR)*, 2016. 2, 3
- [46] Michael Niemeyer, Lars Mescheder, Michael Oechsle, and Andreas Geiger. Occupancy flow: 4d reconstruction by learning particle dynamics. In *Proceedings of the IEEE/CVF international conference on computer vision*, pages 5379–5389, 2019. 2, 3, 4, 6, 7, 8
- [47] Jeong Joon Park, Peter Florence, Julian Straub, Richard Newcombe, and Steven Lovegrove. DeepSDF: Learning continuous signed distance functions for shape representation. In *Proceedings of the IEEE/CVF conference on computer vision and pattern recognition*, pages 165–174, 2019. 2, 6
- [48] Keunhong Park, Utkarsh Sinha, Jonathan T Barron, Sofien Bouaziz, Dan B Goldman, Steven M Seitz, and Ricardo Martin-Brualla. Nerfies: Deformable neural radiance fields. In *Proceedings of the IEEE/CVF International Conference on Computer Vision*, pages 5865–5874, 2021. 4
- [49] Adam Paszke, Sam Gross, Francisco Massa, Adam Lerer, James Bradbury, Gregory Chanan, Trevor Killeen, Zeming Lin, Natalia Gimelshein, Luca Antiga, et al. Pytorch: An imperative style, high-performance deep learning library. *Advances in neural information processing systems*, 32, 2019. 5
- [50] Gerard Pons-Moll, Sergi Pujades, Sonny Hu, and Michael J Black. Clothcap: Seamless 4d clothing capture and retargeting. *ACM Transactions on Graphics (ToG)*, 36(4):1–15, 2017. 2, 3, 6, 7
- [51] Albert Pumarola, Enric Corona, Gerard Pons-Moll, and Francesc Moreno-Noguer. D-nerf: Neural radiance fields

- for dynamic scenes. In *Proceedings of the IEEE/CVF Conference on Computer Vision and Pattern Recognition*, pages 10318–10327, 2021. 4
- [52] Shunsuke Saito, Jinlong Yang, Qianli Ma, and Michael J Black. Scanimate: Weakly supervised learning of skinned clothed avatar networks. In *Proceedings of the IEEE/CVF Conference on Computer Vision and Pattern Recognition*, pages 2886–2897, 2021. 2, 3
- [53] Andrei Sharf, Dan A Alcantara, Thomas Lewiner, Chen Greif, Alla Sheffer, Nina Amenta, and Daniel Cohen-Or. Space-time surface reconstruction using incompressible flow. *ACM Transactions on Graphics (TOG)*, 27(5):1–10, 2008. 2, 5
- [54] J Ryan Shue, Eric Ryan Chan, Ryan Po, Zachary Ankner, Jiajun Wu, and Gordon Wetzstein. 3d neural field generation using triplane diffusion. In *Proceedings of the IEEE/CVF Conference on Computer Vision and Pattern Recognition*, pages 20875–20886, 2023. 2
- [55] Vincent Sitzmann, Julien Martel, Alexander Bergman, David Lindell, and Gordon Wetzstein. Implicit neural representations with periodic activation functions. *Advances in neural information processing systems*, 33:7462–7473, 2020. 6
- [56] Miroslava Slavcheva, Maximilian Baust, Daniel Cremers, and Slobodan Ilic. Killingfusion: Non-rigid 3d reconstruction without correspondences. In *Proceedings of the IEEE Conference on Computer Vision and Pattern Recognition*, pages 1386–1395, 2017. 5
- [57] Justin Solomon, Mirela Ben-Chen, Adrian Butscher, and Leonidas Guibas. As-killing-as-possible vector fields for planar deformation. In *Computer Graphics Forum*, pages 1543–1552. Wiley Online Library, 2011. 5
- [58] Daiwen Sun, He Huang, Yao Li, Xinqi Gong, and Qiwei Ye. Dsr: Dynamical surface representation as implicit neural networks for protein. *Advances in Neural Information Processing Systems*, 36, 2023. 2, 6, 7, 8
- [59] Shanlin Sun, Kun Han, Deying Kong, Hao Tang, Xiangyi Yan, and Xiaohui Xie. Topology-preserving shape reconstruction and registration via neural diffeomorphic flow. In *Proceedings of the IEEE/CVF Conference on Computer Vision and Pattern Recognition*, pages 20845–20855, 2022. 2, 3, 4, 6, 7, 8
- [60] Bin Tan, Zhixiong Ma, Xichan Zhu, Sen Li, Lianqing Zheng, Libo Huang, and Jie Bai. Tracking of multiple static and dynamic targets for 4d automotive millimeter-wave radar point cloud in urban environments. *Remote Sensing*, 15(11):2923, 2023. 1
- [61] Jiapeng Tang, Dan Xu, Kui Jia, and Lei Zhang. Learning parallel dense correspondence from spatio-temporal descriptors for efficient and robust 4d reconstruction. In *Proceedings of the IEEE/CVF Conference on Computer Vision and Pattern Recognition*, pages 6022–6031, 2021. 2, 3
- [62] Michael Tao, Justin Solomon, and Adrian Butscher. Near-isometric level set tracking. In *Computer Graphics Forum*, pages 65–77. Wiley Online Library, 2016. 5
- [63] Edith Tretschk, Vladislav Golyanik, Michael Zollhöfer, Aljaz Bozic, Christoph Lassner, and Christian Theobalt. Scenerflow: Time-consistent reconstruction of general dynamic scenes. In *International Conference on 3D Vision (3DV)*, 2024. 2, 3
- [64] Zhigang Tu, Zhisheng Huang, Yujin Chen, Di Kang, Linchao Bao, Bisheng Yang, and Junsong Yuan. Consistent 3d hand reconstruction in video via self-supervised learning. *IEEE Transactions on Pattern Analysis and Machine Intelligence*, 45(8):9469–9485, 2023. 2
- [65] Daniel Vlasic, Ilya Baran, Wojciech Matusik, and Jovan Popović. Articulated mesh animation from multi-view silhouettes. In *Acm Siggraph 2008 papers*, pages 1–9. 2008. 2, 3
- [66] Tuan-Anh Vu, Duc Thanh Nguyen, Binh-Son Hua, Quang-Hieu Pham, and Sai-Kit Yeung. Rfnet-4d: Joint object reconstruction and flow estimation from 4d point clouds. In *European Conference on Computer Vision*, pages 36–52, 2022. 2
- [67] Thomas Walker, Octave Mariotti, Amir Vaxman, and Hakan Bilen. Explicit neural surfaces: Learning continuous geometry with deformation fields. In *NeurIPS 2023 Workshop on Symmetry and Geometry in Neural Representations*, 2023. 2, 3
- [68] Francis Williams, Matthew Trager, Joan Bruna, and Denis Zorin. Neural splines: Fitting 3d surfaces with infinitely-wide neural networks. In *Proceedings of the IEEE/CVF Conference on Computer Vision and Pattern Recognition*, pages 9949–9958, 2021. 2
- [69] Wenqi Xian, Jia-Bin Huang, Johannes Kopf, and Changil Kim. Space-time neural irradiance fields for free-viewpoint video. In *Proceedings of the IEEE/CVF Conference on Computer Vision and Pattern Recognition*, pages 9421–9431, 2021. 2
- [70] Rui Xu, Zhiyang Dou, Ningna Wang, Shiqing Xin, Shuangmin Chen, Mingyan Jiang, Xiaohu Guo, Wenping Wang, and Changhe Tu. Globally consistent normal orientation for point clouds by regularizing the winding-number field. *ACM Trans. Graph.*, 42(4), 2023. 2
- [71] Haitao Yang, Xiangru Huang, Bo Sun, Chandrajit L Bajaj, and Qixing Huang. Gencorres: Consistent shape matching via coupled implicit-explicit shape generative models. In *The Twelfth International Conference on Learning Representations*, 2023. 2
- [72] Ziyi Yang, Xinyu Gao, Wen Zhou, Shaohui Jiao, Yuqing Zhang, and Xiaogang Jin. Deformable 3d gaussians for high-fidelity monocular dynamic scene reconstruction. In *IEEE Conf. on Computer Vision and Pattern Recognition (CVPR)*, 2024. 2, 3
- [73] Yiming Zeng, Yue Qian, Qijian Zhang, Junhui Hou, Yixuan Yuan, and Ying He. Idea-net: Dynamic 3d point cloud interpolation via deep embedding alignment. In *Proceedings of the IEEE/CVF Conference on Computer Vision and Pattern Recognition*, pages 6338–6347, 2022. 7
- [74] Baowen Zhang, Jiahe Li, Xiaoming Deng, Yinda Zhang, Cuixia Ma, and Hongan Wang. Self-supervised learning of implicit shape representation with dense correspondence for deformable objects. In *Proceedings of the IEEE/CVF International Conference on Computer Vision*, pages 14268–14278, 2023. 2, 3, 5



- [75] Biao Zhang, Jiapeng Tang, Matthias Niessner, and Peter Wonka. 3dshape2vecset: A 3d shape representation for neural fields and generative diffusion models. *ACM Transactions on Graphics (TOG)*, 42(4):1–16, 2023. [3](#)
- [76] Chao Zhang, Sergi Pujades, Michael J. Black, and Gerard Pons-Moll. Detailed, accurate, human shape estimation from clothed 3d scan sequences. In *The IEEE Conference on Computer Vision and Pattern Recognition (CVPR)*, 2017. [2](#), [3](#)
- [77] Qingnan Zhou and Alec Jacobson. Thingi10k: A dataset of 10,000 3d-printing models. *arXiv preprint arXiv:1605.04797*, 2016. [8](#)
- [78] Silvia Zuffi, Ylva Mellbin, Ci Li, Markus Hoeschle, Hedvig Kjellström, Senya Polikovsky, Elin Hernlund, and Michael J. Black. VAREN: Very accurate and realistic equine network. In *IEEE/CVF Conference on Computer Vision and Pattern Recognition (CVPR)*, 2024. [1](#)